

Automatic Ki-67 Counting Using Robust Cell Detection and Online Dictionary Learning

Fuyong Xing*, *Student Member, IEEE*, Hai Su, Janna Neltner, and Lin Yang, *Member, IEEE*

Abstract—Ki-67 proliferation index is a valid and important biomarker to gauge neuroendocrine tumor (NET) cell progression within the gastrointestinal tract and pancreas. Automatic Ki-67 assessment is very challenging due to complex variations of cell characteristics. In this paper, we propose an integrated learning-based framework for accurate automatic Ki-67 counting for NET. The main contributions of our method are: 1) A robust cell counting and boundary delineation algorithm that is designed to localize both tumor and nontumor cells. 2) A novel online sparse dictionary learning method to select a set of representative training samples. 3) An automated framework that is used to differentiate tumor from nontumor cells (such as lymphocytes) and immunopositive from immunonegative tumor cells for the assessment of Ki-67 proliferation index. The proposed method has been extensively tested using 46 NET cases. The performance is compared with pathologists' manual annotations. The automatic Ki-67 counting is quite accurate compared with pathologists' manual annotations. This is much more accurate than existing methods.

Index Terms—Cell detection, classification, Ki-67, neuroendocrine tumor (NET), segmentation.

I. INTRODUCTION

NEUROENDOCRINE tumor (NET) is one of the most common cancers leading to death worldwide. Personalized diagnosis and treatment have significant influences on the survival of the NET patients. Recently, Ki-67 proliferation index, which is represented as the ratio between the numbers of immunopositive tumor cells and all tumor cells, is increasingly considered as a valid biomarker to evaluate tumor cell progression and predicting therapy responses [1]. Manual Ki-67 assessment is subject to a low throughput processing rate and pathologist-dependent bias. Computer-aided pathological image analysis is a promising approach to improve the objectivity and reproducibility. However, it is difficult to access automatic and accurate Ki-67 counting in digitized NET images, since the complex nature of

histopathological images, such as variations of image texture, color, size, and shape, presents significant challenges for accurate automatic Ki-67 counting. In addition, tumor and nontumor cells are usually clustered such that the nontumor cells are also counted using many traditional methods, which lead to large counting errors.

In Ki-67 staining for NET, the color of immunonegative to immunopositive tumor cells ranges from blue to brown (see Fig. 1) in terms of the stage of Ki-67 proliferation. Many computerized methods rely on the color feature to detect and classify cells for Ki-67 scoring. Al-Lahham *et al.* [2] first applied K-means clustering to a transformed color space, and subsequently used mathematical morphology and connected component analysis to segment and count cells on Ki-67 stained histology images. An image analysis system is utilized in [3] to quantify tumor cells, where color intensity thresholds need to be properly selected. In [4], color deconvolution and binarization thresholds are reported for automated assessment of Ki-67 expression in breast cancer. However, it is difficult for these methods to differentiate tumor from nontumor and to handle touching cells. Recently, Nielsen *et al.* [5] first used a MART1 verification strategy to select tumor areas, and calculated cell areas and irregularity to classify positive and negative tumor cells that are obtained by using intensity-based thresholding functions. In [6], an established image analysis software [7] is applied to quantitation of the Ki-67 proliferation index, and multiple staining methods are used to discriminate tumor from nontumor cells. In order to handle touching cells, Loukas *et al.* [8] detected all cells using a Laplacian-of-Gaussian (LoG) filter followed by a distance map transformation for cancer cell counting, and then applied principal component analysis to a transformed color space for immunopositive and immunonegative cells. Markiewicz *et al.* [9], [10] employed the watershed algorithm to separate touching cells and a support vector machine (SVM) classifier to differentiate immunopositive from immunonegative cells, and similar methods are also presented in [11] and [12]. However, these methods cannot precisely differentiate tumor from nontumor cells and separate touching cells simultaneously. The Aperio image analysis software is utilized in [13] and [14] for the assessment of Ki-67 proliferation index, but the nontumor cells such as lymphocytes and stromal cells need to be excluded manually [13], and therefore it is not completely automatic.

Besides the aforesaid methods, more general and sophisticated cell detection algorithms can also be used to estimate Ki-67 proliferation index. Bernardis and Yu [15] formulated cell detection as a spectral graph problem, where pixels are graph nodes and locating cells become dissecting the graph based on

Manuscript received June 13, 2013; revised September 23, 2013 and November 6, 2013; accepted November 8, 2013. Date of publication November 20, 2013; date of current version February 14, 2014. Asterisk indicates corresponding author.

*F. Xing is with the Division of Biomedical Informatics, Department of Biostatistics, and the Department of Computer Science, University of Kentucky, Lexington, KY 40506 USA (e-mail: fuyong.xing@uky.edu).

H. Su and L. Yang are with the Division of Biomedical Informatics, Department of Biostatistics, and the Department of Computer Science, University of Kentucky, Lexington, KY 40506 USA (e-mail: hai.su@uky.edu; lin.yang@uky.edu).

J. Neltner is with the Department of Pathology, University of Kentucky, Lexington, KY 40506 USA.

Color versions of one or more of the figures in this paper are available online at <http://ieeexplore.ieee.org>.

Digital Object Identifier 10.1109/TBME.2013.2291703

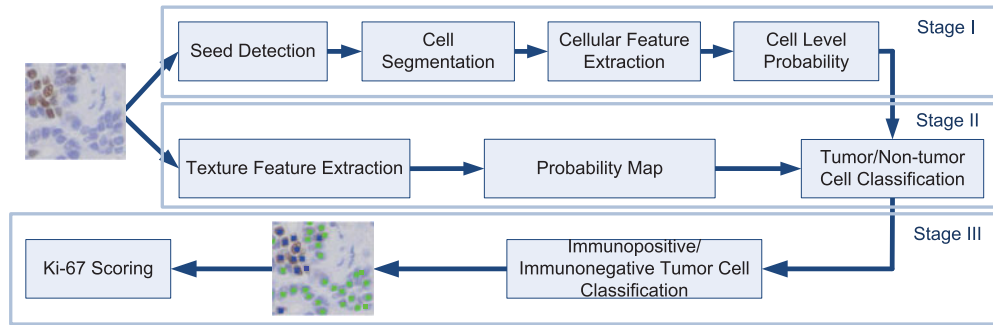


Fig. 1. Workflow of the proposed automatic Ki-67 proliferation index scoring system.

weighted connections between nodes. Another graph-based cell detection and counting method can be found in [16], where a graph-based image representation is first created using luminance information and then a graph mining process is employed to detect the cells. In [17], an object detection and segmentation method based on concavity detection and ellipse fitting is presented for automatic cell counting. Lou *et al.* [18] detected and segmented cell nuclei using blob-like shape prior, and solved an optimization problem in the graph cut framework. A K-nearest neighbor-based graph is proposed in [19] for Ki-67 hot spots detection on glioblastoma, and a voronoi diagram-based nuclei detection and segmentation is presented in [20].

Watershed and its variants are another popular group of cell detection and segmentation methods. Yang *et al.* [21] detected the cell markers based on condition erosion morphology and applied the marker-based watershed to cell segmentation. A supervised learning-based marker detection approach for watershed cell segmentation is presented in [22]. Lin *et al.* [23] proposed a 3-D watershed algorithm incorporating intensity gradient and geometric distance for nuclei segmentation. In [24], an enhanced watershed transform based on flood level thresholds is presented for nuclei detection and segmentation on RNAi fluorescent cellular images. Jung and Kim [25] applied distance transformation-constrained H-minima transform to nuclei detection on cervical and breast cell images, while an adaptive H-minima transform is presented in [26]. Another H-minima transform-based watershed algorithm combined with a region merging technique is proposed in [27] to handle the oversegmentation.

For cells that usually exhibit circular or approximately circular shapes, radial voting has been widely used. Parvin *et al.* [28] proposed an iterative radial voting (IRV) algorithm based on oriented kernels to localize cell nuclei, in which the voting direction and areas are dynamically updated within each consecutive iteration. A computationally efficient single-pass voting (SPV) for cell detection is reported in [29], which applies mean shift clustering instead of iterative voting to final seed localization. Schmitt and Hasse [30] detected individual cells using an iterative kernel voting based on the distance transformation and the local intensities, and another similar iterative voting algorithm for nucleus center detection is reported in [31]. A fast radial symmetry transform is presented in [32] for nuclei localization on H&E stained breast cancer biopsy images.

Another class of methods uses spatial filters to detect cells/nuclei. A LoG filter-based algorithm to automatically detect cell nuclei is presented in [33] and [34]. Bao *et al.* [35] proposed to recognize nuclei for cell tracking using a 3-D spatial filter on *Caenorhabditis elegans*. Supervised learning-based methods are also utilized to automatically localize cells. In [36], a statistical model using nonoverlapping extremal regions is reported to detect cells, while a learned shape model in [37] is employed to localize nuclei. Another learning-based cell detection algorithm [38] is proposed to first segment cluster on histopathology images and then individual cells are obtained by an iterative method based on detected concave points and radial-symmetry centers. Karsnas *et al.* [39] utilized learned intensity and label dictionaries [40] to segment out cells and further split the touching cases using a marker-based watershed algorithm based on cell shapes and areas. The algorithm is tested on two sets of stained images and achieves good performance. Recently, some other techniques are proposed for cell detection. In [41], cell detection for *Myxococcus xanthus* bacteria is achieved using the Hessian matrix and an outer medical axis spike-based method. A spatially constrained EM algorithm with Markov prior is proposed in [42] to detect cell nuclei. More recently, a modified ultimate erosion process is developed in [43] to decompose a mixture of cells into markers, and an edge-to-marker association method is used to identify the set of evidences for cell delineation. Methods based on adaptive thresholds [44], [45] and mode finding [46], [47] are also presented for cell detection. In addition, statistical shape model [48], [49], learning-based deformable model [50], [51], Bayesian inference [52], [53], and shape prior-based level set [54], [55] are reported for object detection and segmentation and achieve high accuracy on specific medical images.

The aforementioned general cell detection and segmentation algorithms are not specifically designed to calculate Ki-67 proliferation index. The nontumor cells such as lymphocytes, stromal, and/or epithelial cells thus often need to be excluded manually. Meanwhile, additional steps need to be designed to separate immunonegative and immunopositive tumor cells. In this paper, we propose an integrated learning-based algorithm (see Fig. 1) for automatic scoring of Ki-67 proliferation index of NET, with addressing the problems earlier simultaneously. In order to accurately and simultaneously localize a large number of cells, we propose a robust and efficient region-based voting algorithm to detect cell seeds (geometric centers). These seeds will be used to

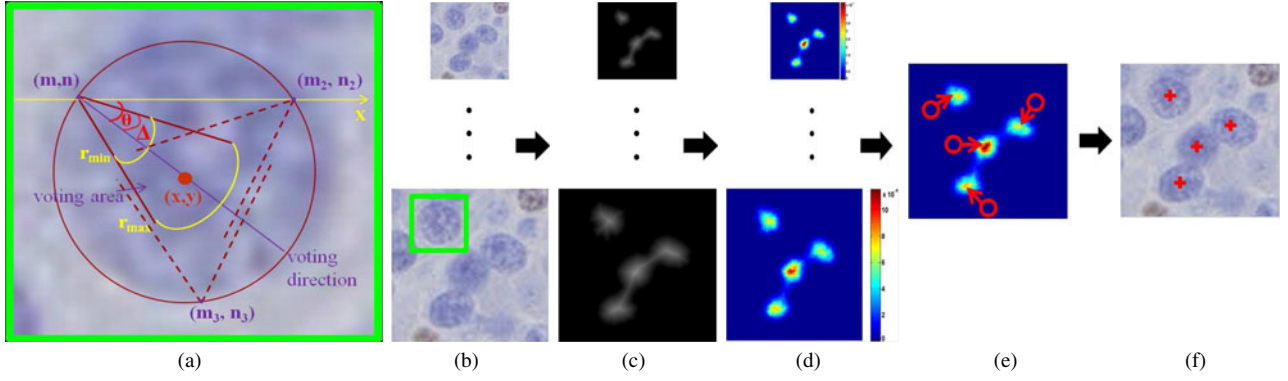


Fig. 2. Procedure of hierarchical voting-based seed detection. (a) Illustration of voting area and direction, (b) original image, (c) distance map, (d) confidence map, (e) mean-shift clustering (the circle represents one point and the arrow denotes the mean-shift vector) on the final confidence map, (f) final seeds. Please note that pixel (x, y) in (a) sums all the voting values created by neighboring pixels $\{(m, n), (m_2, n_2), (m_3, n_3), \dots\}$ whose voting areas contain (x, y) .

initialize a repulsive deformable model to extract touching cell boundaries with known object topology constraints. Next, an efficient online sparse dictionary learning algorithm is applied to select a set of representative training samples. Finally, tumor and nontumor cells are separated by a trained SVM classifier with both the cellular features and regional structure information. The Ki-67 proliferation index is calculated based on the classification results of immunopositive (brown cells in Fig. 1) and immunonegative (blue cells in Fig. 1) tumor cells.

The rest of the paper is organized as follows: Section II presents the automatic Ki-67 counting algorithm. Section III illustrates the experimental results and discussion, and Section IV concludes the paper.

II. METHODS

Our novel integrated learning-based algorithm for automatic Ki-67 scoring of NET contains the following steps: 1) Robust cell detection and boundary delineation followed by cellular features extraction. 2) A learning-based region segmentation algorithm is used to generate a probability map to differentiate tumor and nontumor regions. 3) Both the cellular features and regional structure information are combined to provide accurate tumor cell detection. 4) The Ki-67 proliferation index is finally calculated using a classifier with color histograms to separate immunopositive (brown cells in Ki-67 staining) and immunonegative (blue cells in Ki-67 staining) tumor cells. The whole algorithm flowchart is shown in Fig. 1.

A. Automatic Cell Detection and Boundary Delineation

Robust cell detection is achieved by finding the geometric centers (seeds) of the cells. SPV in [29] localizes the seeds by performing a gradient magnitude-weighted majority vote, but it is not able to efficiently handle cell size and shape variations, since its single voting area and mean shift clustering with a unit bandwidth are not appropriate for different types of cells in one image. For a specific pixel, SPV only sums its own votes without counting those votes from its neighbors, which are important in localizing cell seeds. In addition, the gradient magnitudes are sensitive to noise, and pixels inside the cells may have much smaller magnitudes. Intuitively, the pixels close to cell centers should obtain higher weights than those near cell boundaries. Based on these observations, we introduce a

region-based hierarchical voting in a distance transform map, which applies a Gaussian pyramid to the voting procedure to handle scale variations.

Let $T(x, y)$ denote the original image, and $\nabla T(x, y)$ be the gradient, for each pixel (x, y) at layer l the proposed cell detection algorithm defines its cone-shape voting areas A_l with vertex at (x, y) and votes along the negative gradient direction: $\frac{-\nabla T(x, y)}{\|\nabla T(x, y)\|} = -(\cos(\theta(x, y)), \sin(\theta(x, y)))$, where θ represents the angle of the gradient direction with respect to x -axis. A confidence map $V(x, y)$ is calculated by weighting the distance transform map with a Gaussian kernel $g(m, n, \mu_x, \mu_y, \sigma)$

$$V(x, y) = \sum_{l=0}^L \sum_{(m, n) \in S} I[(x, y) \in A_l(m, n)] \cdot C_l(x, y) g(m, n, \mu_x, \mu_y, \sigma) \quad (1)$$

where S represents the set of all voting pixels, $A_l(m, n)$ denotes the cone-shape voting area with vertex (m, n) at layer l , and it is defined by the radial range (r_{\min}, r_{\max}) and angular range Δ , see Fig. 2(a). $I(x) = I[(x, y) \in A_l(m, n)]$ is the indicator function, and $C_l(x, y)$ represents the distance transformation map at layer l , which can be the Euclidean distance transform. The isotropic Gaussian kernel is parametrically defined with $(\mu_x, \mu_y) = (x + \frac{(r_{\max} - r_{\min}) \cos \theta}{2}, y - \frac{(r_{\max} - r_{\min}) \sin \theta}{2})$ and scalar σ , which is used to encourage the voting toward the cell central regions. Fig. 2(c) shows that pixels with higher $C_l(x, y)$ values near the geometric center of a cell will enhance their contributions in (1). For each pixel (x, y) , (1) provides a weighted sum of all the voting values created by its neighboring pixels whose voting areas contain (x, y) [see Fig. 2(a)], instead of only counting those votes created by its own. After the confidence map is generated [see Fig. 2(e)], mean shift [56] is employed to calculate the final seed for each individual cell, see Fig. 2(f). In comparison with SPV, hierarchical voting is more robust with respect to the detection of cells with relatively large size variations.

The proposed cell detection algorithm indiscriminately detects both tumor and non-tumor cells, and therefore, the results cannot be directly used to calculate the Ki-67 proliferation index. Differentiation between tumor and nontumor cells is the critical step for accurate automatic Ki-67 scoring. In order to

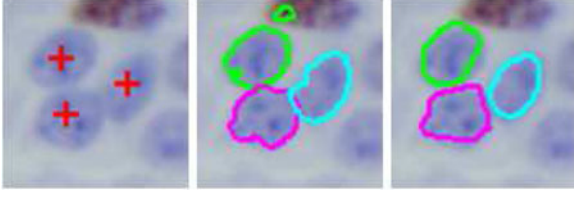


Fig. 3. Left: Seed detection used to initialize repulsive level set [24] and the proposed model. Middle and Right: Cell segmentation result using the repulsive level set and the proposed repulsive balloon snake. Please note that repulsive level set splits the green contour into two disconnected contours, and therefore creates a small hole on the top of the figure, while the repulsive balloon snake can precisely preserve the known object topology. It only generates three contours given three seeds.

extract distinctive morphological features to separate tumor from nontumor cells, accurate cellular boundary delineation is a prerequisite. This is a challenging problem due to the complex color and intensity variations inside the cells, especially within touching cell clumps. Based on the cell detection results, we propose to describe cell boundaries by segmenting each individual cell with an improved deformable model.

We introduce a contour-based repulsive term into the deformable model [57] to prevent evolving contours from crossing and merging with one another. For each cell, the model deforms the contour $v_i(s)$ until it achieves a balance between the internal $F^{\text{int}}(v_i)$ and external $F_R^{\text{ext}}(v_i)$ forces: $F^{\text{int}}(v_i) + F_R^{\text{ext}}(v_i) = 0$

$$F^{\text{int}}(v_i) = \alpha v_i''(s) - \beta v_i'''(s) \quad (2)$$

$$F_R^{\text{ext}}(v_i) = \gamma \mathbf{n}_i(s) - \lambda \frac{\nabla E_{\text{ext}}(v_i(s))}{\|E_{\text{ext}}(v_i(s))\|} + \omega \sum_{j=1, j \neq i}^N \int_0^1 d_{ij}^{-2}(s, t) \mathbf{n}_j(t) dt \quad (3)$$

where the two terms in (2) are the second and fourth derivative of $v_i(s)$ with corresponding weights α and β , respectively. The $\mathbf{n}_i(s)$ together with weight γ in (3) represents the pressure force, and $\nabla E_{\text{ext}}(v_i(s))$ denotes the image force where $E_{\text{ext}}(v_i(s)) = -\|\nabla T[x(s), y(s)]\|^2$.

Our newly introduced term (last term) in (3) represents the repulsive force, where N is the number of cells, $d_{ij}(s, t) = \|v_i(s) - v_j(t)\|_2$ denotes the Euclidean distance between contour $v_i(s)$ and $v_j(t)$. The parameter ω controls the weight for the repulsive force. Using the previously detected seed as initializations, this repulsive deformable model can handle touching cells effectively. In order to prevent numerical instability, the repulsive force near $d_{ij} = 0$ is clipped and set as the one with $d_{ij} = 1$.

Compared with [54], [55], [58] that introduce an area-based penalty term to avoid contour overlapping, we design a contour-based model to improve the computational and memory efficiency. In addition, there are several major differences: 1) Similar to the design of the geometric snake models [24], [59]–[61], the model in [55] is formulated within the level set framework that allows topological changes. This feature, although sometimes can provide desirable properties, may introduce false holes especially in the inhomogeneous regions inside or outside the cell (see Fig. 3). On the other hand, the proposed parametric repulsive deformable model can preserve known object topology,

TABLE I
MORPHOLOGICAL FEATURES FOR THREE-STAGE LEARNING-BASED CLASSIFICATION

Stage	Feature Set	Number	Features
I	Geometric descriptor	5	area, perimeter, circularity, axis ratio*, solidity
	Color intensity	9×3	mean, standard deviation, smoothness†, skewness, kurtosis, entropy, contrast, correlation, homogeneity
	Cell shapes	80	Fourier shape descriptor [62]
II	Probability	4	mean/standard deviation of pixel-based probabilities in each cell, ratio between total pixel level probability for one cell and average pixel-wise probability for all cells in the local region, cellular probability obtained from Stage I
III	Intensity histogram	16×3	A 16-bin intensity histogram is computed for each channel

* axis ratio means the ratio between long and short axis,

† smoothness is calculated as $1 - 1/(1+\text{variance})$.

and therefore each evolving contour only represents one cell without splitting or merging. This topology preserving feature makes the proposed method relatively more robust to inhomogeneous regions inside the cell. 2) The method in [55] utilizes watershed-based results to initialize the following level set evolution. The watershed can create a lot of oversegmented regions, but in our algorithm, we specifically designed a robust hierarchical voting method to provide robust seeds to initialize and guide the proposed topology preserving parametric deformable models to move contours toward the cell boundaries.

B. Training Sample Selection and Online Dictionary Learning

Based on the results of cellular segmentation, a classifier can be trained to determine the segmented cell category (tumor or nontumor cells) with the following cellular features in (listed in Table I Stage I): geometric descriptors, color intensity, and cell shapes that are represented by Fourier shape descriptor [62]. In total, we have extracted $p = 5 + 9 \times 3 + 80 = 112$ features, where 3 represents R , G , and B color channels, and 80 denotes the first 20 harmonics (each corresponds to four coefficients) that are chosen in the Elliptical Fourier transformation.

For more efficient and robust training, we propose to choose a set of representative samples that can approximate the entire training set. This is a data summary problem that can help to reduce the number of training samples, improve the computational efficiency, and more important, to increase the robustness by removing outliers from the original training set. A K-selection dictionary learning algorithm [63] is chosen to select K representatives $\{\phi_k \in R^{W \times 1}\}$ to form a dictionary $\Phi \in R^{W \times K}$ from the original dataset

$$\min_{\{\phi_k\}} \sum_{i=1}^N \left\| f_i - \sum_{k=1}^K \phi_k \xi_{ik} \right\|_2^2 + \theta \left\| e_i \odot \xi_i \right\|_2^2 \quad (4)$$

s.t. $\mathbf{1}^T \xi_i = 1, \forall i$

where ϕ_k is the k th basis vector selected from the original training sample set, $f_i \in R^{W \times 1}$ denotes the i th feature vector, $\xi_i \in R^{K \times 1}$ is the sparse coefficient with a weight θ , and $e_i \in R^{K \times 1}$ represents the distance between f_i and the basis vectors. Unlike the popular sparse dictionary learning method KSVD [64], where the dictionary bases are not consisted with the original samples, (4) enforces the bases to be directly selected from the dataset.

The training data often do not come in one batch. Instead, they are often collected from different pathologists in different institutes in a sequential mode. It is not only time consuming but also impractical to retrain the dictionary whenever new training samples arrive. To deal with training in a sequential mode, the dictionary Φ is required to be online updated for classification. Recreation of the dictionary using the whole dataset including the old $\{f_i\}, i = 1, 2, \dots, N$ and new $\{f_i^{\text{new}}\}, i = 1, 2, \dots, M$ data are neither efficient nor feasible. Because the selected K representatives can efficiently describe the old dataset, it is sufficient to evaluate whether or not Φ are good representatives for $\{f_i^{\text{new}}\}$. Thus, we can solve the optimization problem on a reduced dataset

$$\min_{\{\phi_k\}} \sum_{i=1}^{M+K} \left\| f_i^{\text{new}} - \sum_{k=1}^{K'} \phi_k \xi_{ik} \right\|_2^2 + \theta \left\| e_i \odot \xi_i \right\|_2^2 \quad (5)$$

s.t. $\mathbf{1}^T \xi_i = 1, \forall i$

where $\{f_i^{\text{new}}\}, i = 1, 2, \dots, M$ are the new data, and $\{f_i^{\text{new}}\}, i = M+1, M+2, \dots, M+K$ are the previously selected representatives Φ . K' denotes the number of the representatives need to be selected for the new dataset that contains both old and new training samples. The data size in (5) is $M+K$ which is much smaller than $M+N$ (N represents the size of the original training dataset), and hence the optimization problem in (5) can be solved more efficiently. The online learning strategy enables the dictionary to be properly scaled up to represent a dynamic set of samples while still keeping the efficiency.

C. Three-Stage Learning-Based Classification

After an accurate segmentation and dictionary learning of all the cells in NET, a three-stage learning-based scheme combining cellular features and regional structure information is designed to differentiate tumor from nontumor cells, and immunopositive from immunonegative tumor cells for accurate Ki-67 counting. The reasons why we use multiple stages to calculate Ki-67 proliferation index are: 1) Speed: first, it is much easier and faster to compute cellular features in Stage I than the texture in Stage II. Second, many typical nontumor cells will achieve relatively low-category probabilities using the simple cellular feature-based classifier in Stage I and can then be removed to avoid further processing. The subsequent classifiers will only need to focus on difficult cases. This cascade pipeline structure can dramatically improve the speed. 2) Flexibility: the feature computation in Stages I and II are independent, and either one can be replaced with other methods without changing the whole framework. 3) Evaluability and clinical purpose: in this pipeline framework, all intermediate results can be easily exported and

presented to doctors for evaluation and clinical purpose. 4) Scalability: we have specifically designed these three-stage pipeline structure instead of an integrated module like classification tree considering future parallel implementation using grid and/or cloud.

Stage I: As shown in Table I, we have extracted 112 features for each sample. In order to select the most discriminative features for cell classification, a sparse representation model is applied to the original feature space

$$\min_{b, b_0} \frac{1}{N} \sum_{i=1}^N \log(1 + e^{-a_i(b^T \phi_i + b_0)}), \text{ s.t. } \|b\|_1 \leq \eta, b \succeq \mathbf{0} \quad (6)$$

where $N = N^+ + N^-$ represents the number of training samples containing N^+ tumor and N^- nontumor cells, and $\phi_i \in R^{W \times 1}$ is the extracted feature with $W = 112$ denoting the original dimension. b_0 is the intercept and η represents the sparsity parameter. The binary vector $a \in \mathbb{R}^{(N^+ + N^-) \times 1}$ represents the labels of cells used for training: $a_i = +1$ for tumor and $a_i = -1$ for nontumor. Due to the l_1 norm constraint, the solution $b^* \in \mathbb{R}^{W \times 1}$ to (6) is sparse with nonzero elements corresponding to the selected discriminative features. Based on b^* with L nonzero elements, we can project all the features onto a low-dimensional discriminative subspace. An SVM classifier is learned to predict the cell category in this transformed sparse feature space. We remove those cells with low probabilities that often correspond to typical nontumor cells before the cell classification, such that the second classifier would focus on a reduced dataset. Please note that Stage I will only utilize the training data selected in Section II-B.

Stage II: In Stage I, only cellular features are considered, and some nontumor cells (like lymphocytes) can be classified as tumor cells by mistake. The lymphocytes usually exhibit certain structural pattern on the specimens, which can be described with local structural features. To improve the classification accuracy, texton [65] feature is utilized to model the different structural level features between nontumor and tumor regions. A multiple scale Schmid filter bank [66] is used for image filtering

$$H(r, \sigma, \tau) = H_0(\sigma, \tau) + \cos\left(\frac{\pi r \tau}{\sigma}\right) e^{-\frac{r^2}{2\sigma^2}} \quad (7)$$

where τ is the number of cycles of the harmonic function within the Gaussian envelop of the filter and $r = \sqrt{x^2 + y^2}$. A texton library is constructed using K-means on 20 randomly selected NET specimens using the image filtering results with Schmid filter bank. Considering computational efficiency, an integral histogram [67] is utilized to calculate the multiscale windowed texton histogram. Finally, the logistic boost [68] is employed to calculate the probability map using the multiscale texton histograms as features.

Using the texture classification-based probability map, each individual cell will obtain a score to evaluate its probability belonging to tumor or nontumor cells (see Table I). In addition, the ratio between the probability of one cell and the probability average for all its neighboring cells provides a measurement of cell category distribution. As one can expect, the lymphocyte regions will exhibit higher probability to be classified as nontumor patterns, which can be discarded before Stage II. In this way, the

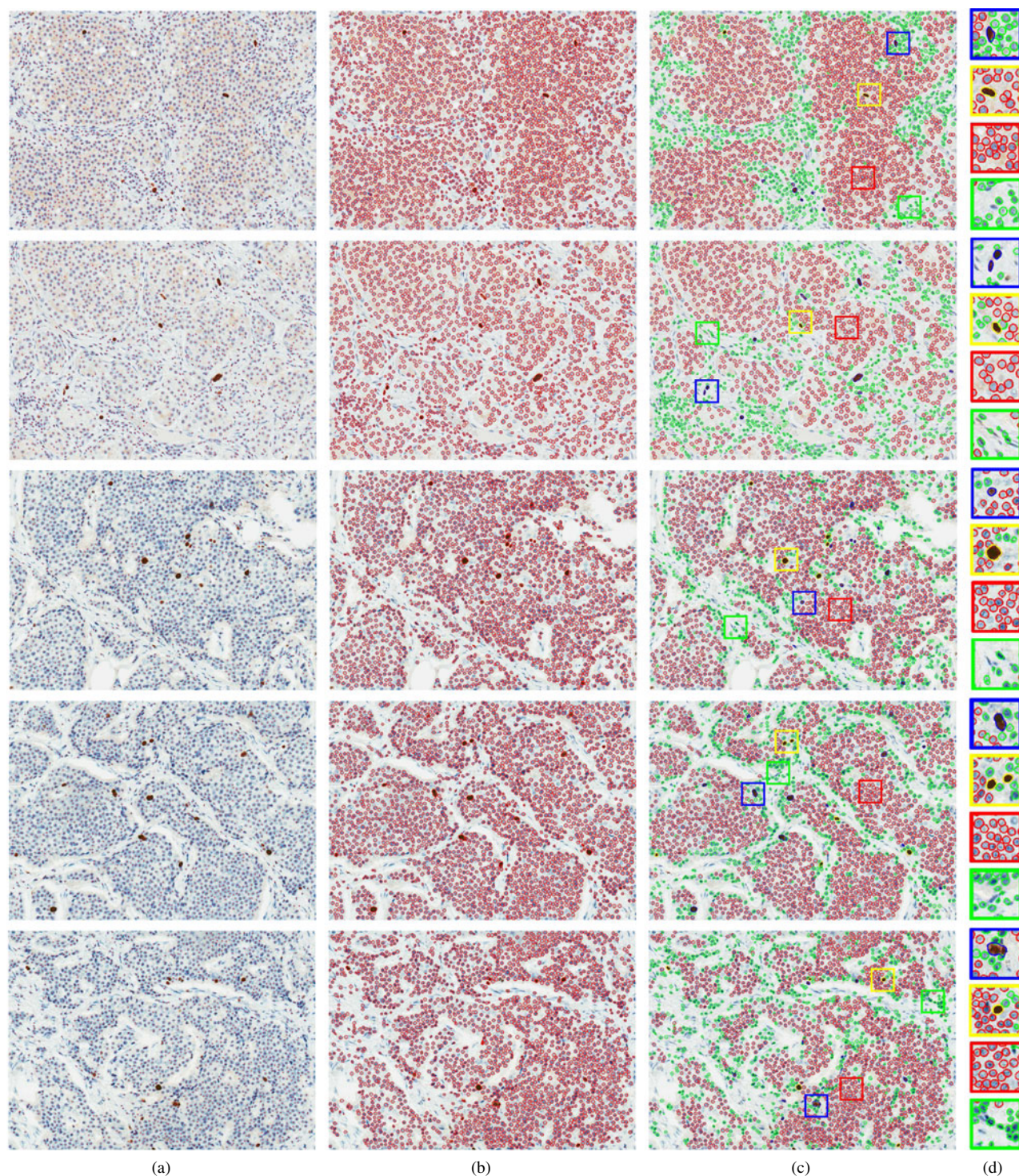


Fig. 4. Results of (a) cell detection, (b) segmentation, and (c) classification on several randomly selected image patches. Some small patches are zoomed in for better illustration in (d). Cells with yellow/red contours represent immunopositive/immunonegative tumor cells. Those with green and blue contours denote nontumor (including lymphocytes or nonlymphocytes) cells, which are recognized by the trained classifiers in Stage II and III, respectively. Some cells (e.g., lymphocytes) without any markers denote that they are excluded in cell detection stage. Please note that we did not count the cells touching with image boundaries on purpose.

classifier in Stage II will focus more on the challenging cases. This improves both computational efficiency and classification accuracy.

In Stage II, the mean/standard deviations of pixel probabilities in each cell, and the percentage of probability summation of one

cell over the probability average for all cells in its local region are calculated. These statistical features are concatenated with the previously predicted cellular probabilities in Stage I to train a second SVM classifier. The output will produce the labels to differentiate tumor from nontumor cells.

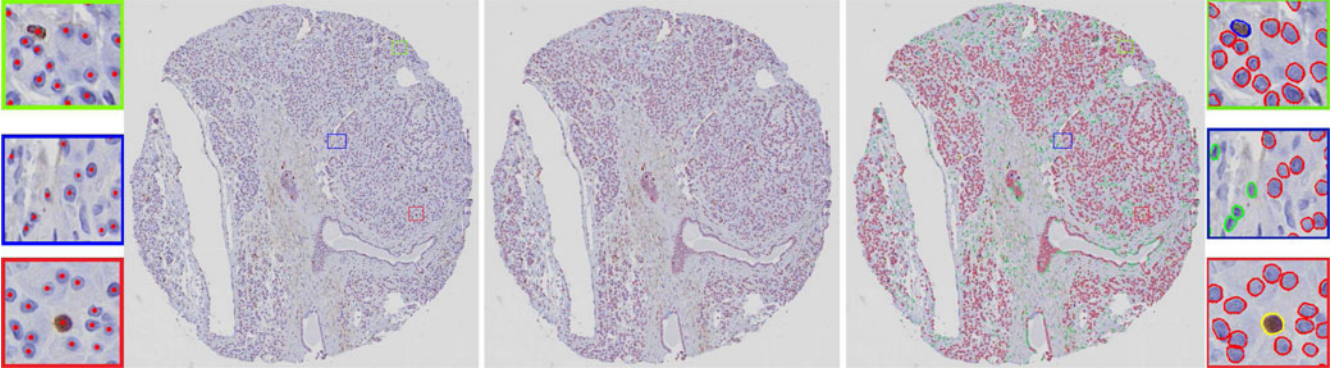


Fig. 5. Cell detection (left), segmentation (middle), and classification (right) using the proposed method on one tissue microarray disc. Several patches are zoomed in for better illustration for the detection and classification. The cells with different colors in the leftmost and rightmost panels have the same meanings as those in Fig. 4.

Stage III: Based on the classification in Stage II, the final step is to separate immunopositive from immunonegative tumor cells. This is achieved by training a final classifier for all the Ki-67 positive staining cells using the features listed in Stage I in Table I, and cellular intensity histogram (a 16-bin intensity histogram separately for each channel, as shown in Stage III in Table I) to differentiate the immunopositive and immunonegative tumor cells.

III. EXPERIMENTAL RESULTS AND DISCUSSION

The proposed algorithm is extensively tested on 46 NET cases with each case corresponding to two or three images, which are captured at $20\times$ magnification. In total, we have 129 images. For each case, we guarantee at least 2000 mixed tumor and nontumor cells are included. All the data are collected from the Department of Pathology at University of Kentucky. Board-certified pathologists have spent several weeks in annotating all the 129 images. We randomly select 20 image for training and the rest is used for testing. The cell detection and classification algorithms are implemented with C/C++. MATLAB is used for cell segmentation on a PC machine with 3.3-GHz Intel i3 CPU and 16-GB memory. The parameters are: $\sigma = 0.3$, $l = 2$ in (1), $\alpha = 0.05$, $\beta = 0$, $\gamma = 0.5$, $\lambda = 5$, $w = 0.7$ in (2), (3), $\theta = 0.0001$ in (4), (5), and $\eta = 80$ in (6).

A. Cell Detection

Both qualitative and quantitative analyses are conducted for the proposed cell detection algorithm. In Fig. 4, thousands of cells are correctly detected and segmented on several randomly selected image patches, which contains both tumor and nontumor cells. We also test our method on one sample tissue microarray disc, as shown in Fig. 5. The computational time for a digitized 2310×2150 image is only 96.5 s without any specific optimization, which indicates the efficiency of our cell detection algorithm compared with 30-min manual counting by pathologists.

The proposed method is compared with four recent state of the arts: LoG filters [33], IRV [28], SPV [29], and ITCN [34], and the results are shown in Fig. 6. As one can see, it is difficult for LoG and ITCN to handle inhomogeneous in-

tensity and touching cells. LoG and ITCN falsely detect some seeds on cell boundaries and in the background, respectively, so they could have a relatively high false detection. IRV and SPV may fail on elongated cells due to the assumption of approximate circular objects. In addition, it is not easy for IRV and SPV to create a general rule for parameter selection on one single image containing cells with different sizes and shapes. However, the proposed algorithm is more robust with respect to the variations of cell scale and intensity. This can be attributed to the region-based hierarchical voting on the distance map.

To quantitatively evaluate seed detection accuracy, we measure the Euclidean distances between manually located seeds and those created by automatic algorithms in Table II. It is clear that LoG is outperformed by the other three methods, and ours produces the best performance. The reason that IRV, SPV, and ours give approximately equal pixel-wise detection accuracy is because we did not consider the cases of under- (UR) and over-detection (OR).

In order to evaluate the detection accuracy in a more effective manner, we have defined the following rigorous metrics to evaluate automatic cell detection accuracy: 1) UR, shown in Fig. 7(b): No seeds are detected inside a circular region with a radius $r = 4$ pixels centered at the ground-truth seed. 2) OR, shown in Fig. 7(c) and (d): More than one seed are detected inside the central circular region. 3) Effective rate (ER): The ratio between the number of detected seeds and ground-truth seeds, which is used to measure the methods' robustness to background clutter. $ER = 1$ indicates the strongest robustness. Table III shows the comparative performance the rates of UR/OR and the ER. LoG and IRV miss some cells, and ITCN is relatively sensitive to noises on the image background. The SPV can produce better results, but it is outperformed by the proposed method. We also quantitatively evaluate the proposed method using precision (P), recall (R) and F_1 score, which are defined as $P = \frac{TP}{TP+FP}$, $R = \frac{TP}{TP+FN}$, and $F_1 = \frac{2*P*R}{P+R}$. True positive (TP) is defined as a detected seed that is inside the central circular region of the ground-truth seed, see Fig. 7(a). False positive (FP) is defined as the cases that at least one seed is detected outside this circular region but inside the local rectangle region (2-pixel extension from the cell contour in the vertical and horizontal directions), as shown in Fig. 7(d)–(h). False

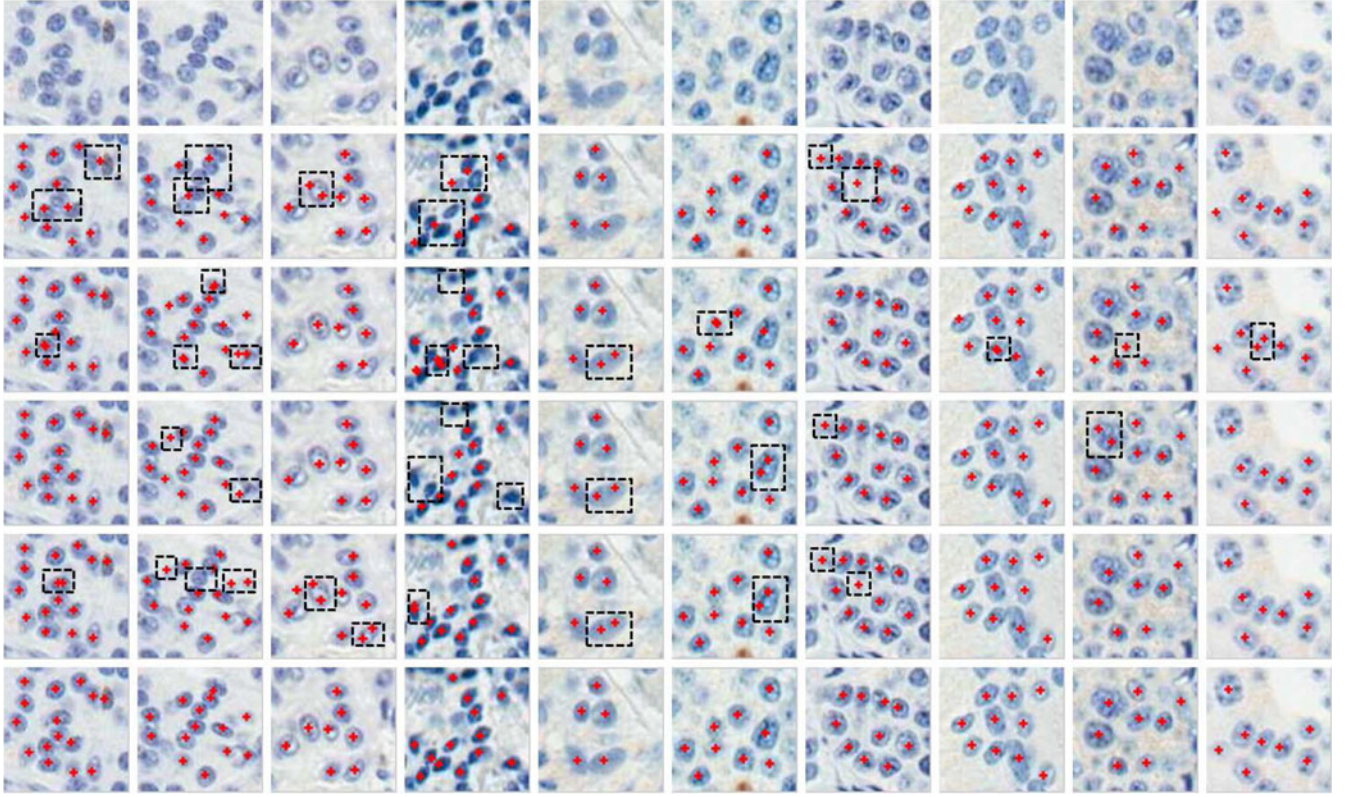


Fig. 6. Geometric centers of cells (seeds) detection on several randomly selected image patches. Row 1 is the original image patches. Rows 2, 3, 4, 5, and 6 correspond to the automatic detection results produced by LoG [33], IRV [28], SPV [29], ITCN [34], and the proposed algorithm, respectively. The missing or false seeds are highlighted with black dashed rectangles.

TABLE II
PIXEL-WISE SEED DETECTION ACCURACY COMPARED
WITH GROUND-TRUTH ANNOTATIONS BY PATHOLOGISTS

	<i>Mean</i>	<i>Variance</i>	<i>Min</i>	<i>Max</i>
LoG [33]	2.72	1.05	0.12	4.95
IRV [28]	1.94	1.14	0.11	4.97
SPV [29]	1.82	1.20	0.07	4.98
ITCN [34]	2.02	1.39	0.11	4.97
Proposed	1.72	0.06	0.01	4.84

TABLE III
COMPARATIVE SEED DETECTION RESULTS EVALUATED
USING DIFFERENT METRICS

	<i>UR</i>	<i>OR</i>	<i>ER</i>	<i>P</i>	<i>R</i>	<i>F1</i>
LoG [33]	0.14	0	1.08	0.75	0.82	0.78
IRV [28]	0.14	0.06	1.11	0.85	0.83	0.84
SPV [29]	0.10	0	1.05	0.88	0.88	0.88
ITCN [34]	0.05	0.02	1.26	0.78	0.93	0.86
Proposed	0.07	0	1.02	0.89	0.91	0.90

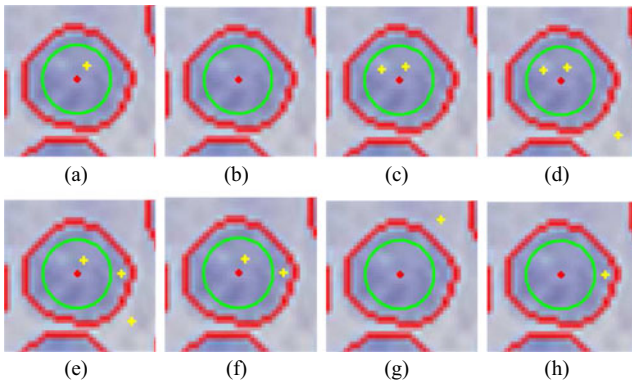


Fig. 7. Definition of quantitative evaluation metrics. The red dot is the doctor's annotation. The green circle represents the ground truth region. Any seed that locates inside the green circle will be treated as correct detection (TP). Red contours are cell boundaries. The yellow crosses denote the automatic detected results. TP (a), FN/underdetection (b), OR (c) (d), and FP (d)–(h) are presented in this Figure. Please note that the case (d) belongs to both OR and FP. Larger circular regions ($r > 4$) and local rectangle regions are used for illustrative purpose.

negatives (FN) are defined as the underdetections [see Fig. 7(b)]. As shown in Table III, LoG and ITCN have relatively lower precision and IRV has higher FN, while SPV and ours produce the best performance.

B. Ki-67 Scoring

In the experiments at Stage I, circularity ratio, axis ratio, color mean, standard deviation, kurtosis, contrast, correlation, and homogeneity are selected by the sparse representation model as the most discriminative features to separate tumor from nontumor cells. This indicates that for Ki-67 staining, tumor cells intend to exhibit more circular shapes than nontumor cells. Nontumor cells often have more inhomogeneous textures and lighter staining. The first SVM classifier uses a Gaussian kernel (the parameter $\sigma = 0.3$ and the penalty $c = 1$) with these selected discriminative features.

Combined with the texton histogram-based probabilities, a second SVM classifier is trained to separate tumor and nontumor

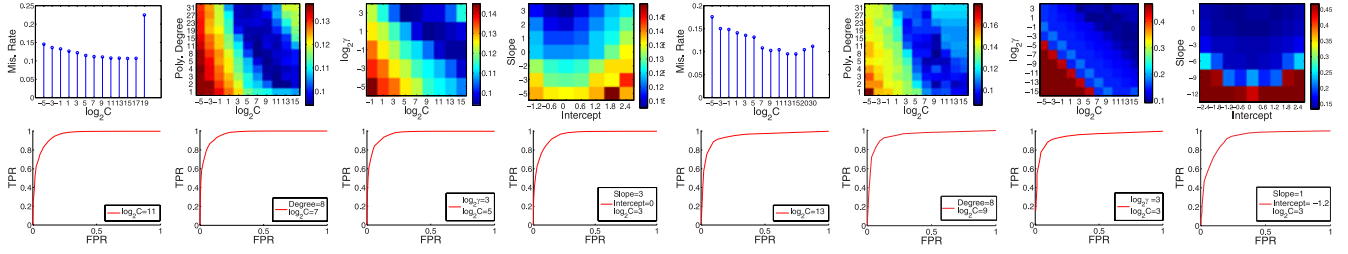


Fig. 8. Misclassification rates (row 1) and corresponding ROC curves (row 2) with respect to different parameters using different kernels to separate tumor and nontumor cells (left four-column panel), and immunopositive and immunonegative tumor cells (right four-column panel). From left to right, each panel represents linear, polynomial, Gaussian, and sigmoid kernels, respectively. In row 1, Mis. Rate and Poly. Degree represent misclassification rate and polynomial degree, respectively. In row 2, TPR/FPR means TP/FP rate.

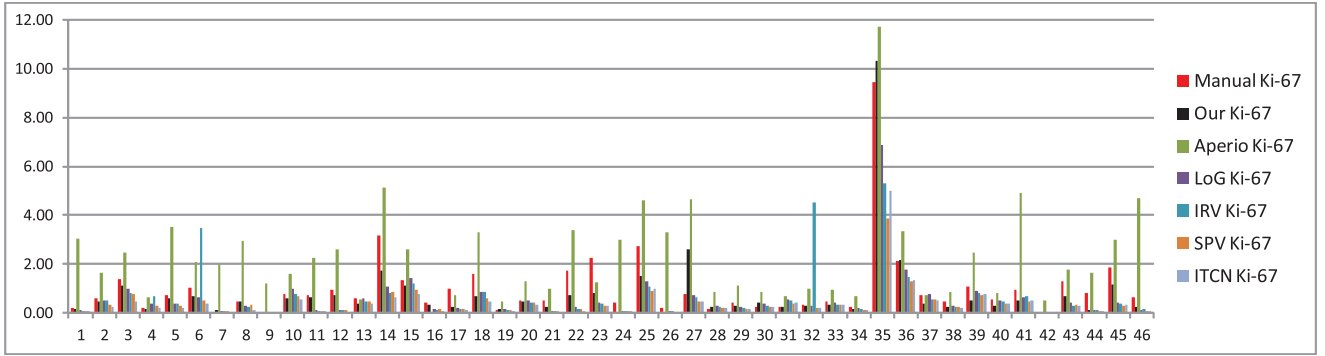


Fig. 9. Manually calculated Ki-67 proliferation index compared with the automatic Ki-67 proliferation index generated by different methods for 46 patients.

cells. Threefold cross validation is applied to evaluate the classifier with respect to parameters on four different kernels, shown in the left four columns of Fig. 8. For linear, polynomial, and Gaussian kernels, the misclassification rates will be relatively high with too small or large penalty C , which corresponds to the cases of underfitting or overfitting, respectively. We can also observe that the kernel parameters (polynomial order or precision γ for Gaussian kernel) interact with the model complexity. For the sigmoid kernel, we keep the penalty fixed (penalty = 8) and calculate the errors by tuning up the slope and the intercept. We found that the sigmoid with relatively large slopes can produce slightly better performance than linear kernel, but it is outperformed by the polynomial and Gaussian kernels. With the optimal parameters, we apply the selected models to the testing samples, and display the ROC curves with different kernels in the second row of Fig. 8. The accuracy, specificity, and sensitivity are 90.2%, 88.8%, 91.6% and 90.2%, 89.6%, 90.8% for polynomial and Gaussian kernels, better than those using linear and sigmoid kernels, with 85.4%, 93.6%, 77.0% and 88.2%, 86.2%, 90.3%, respectively. The same procedure is applied to classify immunopositive and immunonegative tumor cells (shown in the right four columns of Fig. 8), and similar performance is achieved with respect to parameters with different kernels. Based on threefold cross validation, the accuracy, specificity, and sensitivity are 89.9%, 90.3%, 89.4%, 90.3%, 90.3%, 90.2%, and 90.1%, 90.0%, 90.2% for linear, polynomial, and Gaussian kernels, respectively, which are better than the sigmoid kernel with 83.8%, 86.2%, 81.2%. The results demonstrate that a Gaussian or polynomial kernel with proper parameters can

achieve high accuracy and specificities without sacrificing the sensitivities.

Fig. 9 displays the automatic calculated Ki-67 proliferation index based on the classification using a Gaussian kernel with parameters $\log_2 C = 3$ and $\log_2 \gamma = 3$, Aperio's Ki-67 counting, and the Ki-67 calculation results using LoG, IRV, SPV, and ITCN as the cell detection algorithm. The comparison is also displayed on several randomly selected patches in Fig. 10. As we can see, the proposed algorithm outperforms all the other four methods due to precise cell detection and classification performance. Fig. 11 shows the absolute errors between the automatic and manual Ki-67 scores on the 46 cases. Our method not only produces best performance in terms of the mean values, but also gives smaller variance, which demonstrates the strong robustness of the proposed automatic Ki-67 counting algorithm. The reasons are: 1) our method can reliably separate touching cells, and 2) many lymphocytes are not discriminated from the true immunopositive tumor cells in existing methods, while in our algorithm these lymphocytes are correctly recognized based on accurate cellular level segmentation and classification.

We also evaluate the performance of our system by comparing the sparse representation-based model with the data-driven feature selection method, support vector machine recursive feature elimination (SVM-RFE) [69]. Table IV shows the statistics of absolute errors of Ki-67 scoring between the different models and manual counting on the testing data, and the 80% column denotes the sorted 80% largest error of all the results, which is commonly used by doctors to evaluate the usability of the system. As we can see, our method produces similar

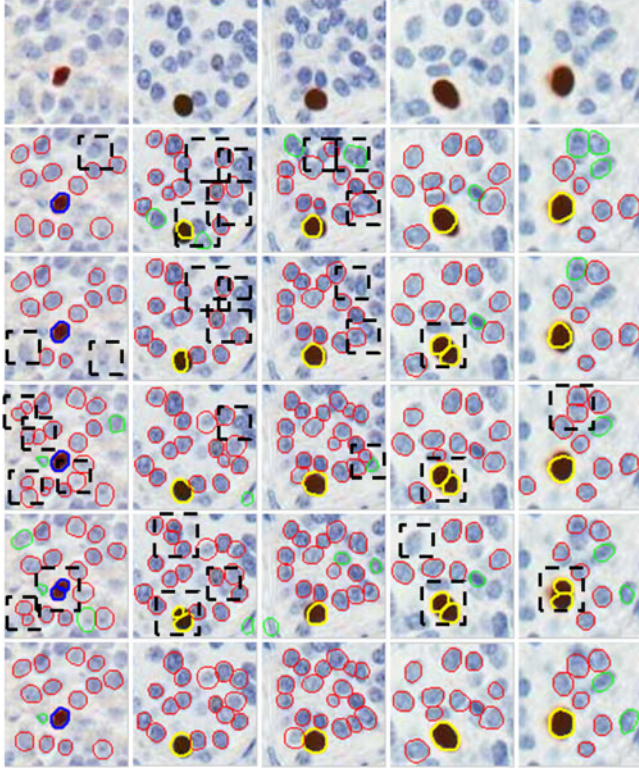


Fig. 10. Effects of different cell detection methods in Ki-67 score computation on several randomly selected image patches. Row 1 is the original image patches. Rows 2, 3, 4, 5, and 6 correspond to LoG [33], IRV [28], SPV [29], ITCN [34], and the proposed algorithm, respectively. The false detection resulting in incorrect Ki-67 computation is highlighted with black dashed rectangles. The colors have the same meaning as those in Fig. 4.

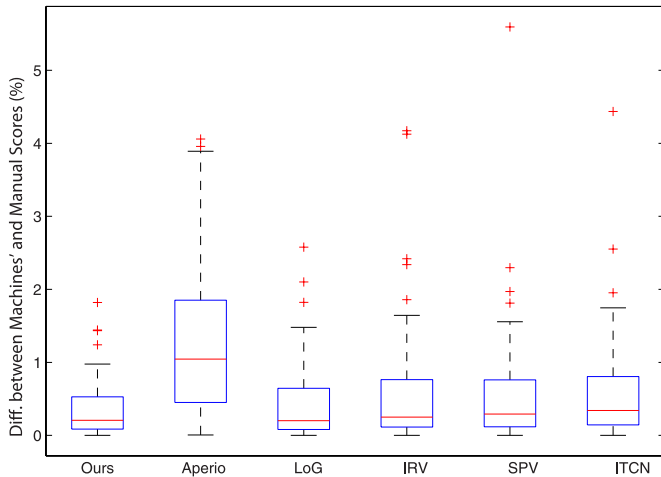


Fig. 11. Absolute errors between manually and automatically generated Ki-67 proliferation index.

TABLE IV
ANALYSIS OF Ki-67 SCORING WITH DIFFERENT MODELS

	<i>Mean</i>	<i>Variance</i>	<i>Min</i>	<i>Max</i>	80%
SVM-RFE [69]	0.37	0.16	0	1.60	0.64
MCSVM	0.37	0.20	0	1.96	0.58
OURS	0.34	0.17	0	1.80	0.52

TABLE V
ASSESSMENT OF Ki-67 PROLIFERATION INDEX WITH RESPECT TO DICTIONARY SIZE

	<i>Mean</i>	<i>Variance</i>	<i>Min</i>	<i>Max</i>
1%	0.36	0.14	0	1.36
5%	0.38	0.21	0	2.24
10%	0.39	0.22	0	2.34
15%	0.38	0.29	0	3.19
20%	0.34	0.17	0	1.8

variance as but lower average and 80% errors than SVM-RFE. The performance of multiclass SVM (MCSVM) with a Gaussian kernel is also presented in Table IV, and it is outperformed by SVM-RFE and ours as well. Although MCSVM gives similar mean error of Ki-67 score as SVM-RFE, it produces relatively larger numbers of both tumor and immunopositive tumor cells. In addition, the average running time of one image for MCSVM with C programming language is approximately two times higher than ours (about 0.2 s).

In order to demonstrate the effect of dictionary size (the number of selected samples in the dictionary learning stage) on the assessment of Ki-67 proliferation index, we calculate the Ki-67 score with different dictionary sizes on the annotated samples, as shown in Table V. The selected percentages are 1%, 5%, 10%, 15%, and 20%. As one can tell, automatic Ki-67 scoring accuracy is not sensitive to the size of the dictionary. This is because a small number of selected samples based on the robust K-selection can already sufficiently represent the whole dataset.

IV. CONCLUSION

The significance of the accurate estimation of Ki-67 proliferation index is obvious. In current classification systems, namely the European Neuroendocrine Tumor Society (ENETS) and the World Health Organization, NETs were separated into three prognostically significant grades: low, intermediate, and high. Such stratification requires the documentation of mitotic counts and/or Ki-67 proliferation index. Low grade (grade 1) NETs have a mitotic count of less than two mitoses/ten high-powered fields (HPF) and/or a Ki-67 index of less than 3%. Intermediate (grade 2) NETs have a mitotic rate of 2–20 mitoses/ten HPF and/or a Ki-67 index of 3–20%. High-grade (grade 3) NETs are morphologically anaplastic, and often show mitotic rates greater than 20 mitoses/ten HPF and Ki-67 index well above 20%. As one can tell, these specific cutoffs (3% and 20%) need to be precisely determined in order to differentiate low, intermediate, and high grades of NETs. The precise tumor grading significantly impacts the diagnosis and prognosis accuracy of NETs.

In this paper, we have introduced an automatic algorithm for Ki-67 scoring of digitized NET images. The novel cell detection algorithm can efficiently and accurately detect thousands of cells on a digitized NET image with Ki-67 staining. Furthermore, a three-stage learning-based approach is designed to differentiate tumor cells from nontumor cells and immunopositive and immunonegative tumor cells for an automatic, accurate, and robust quantification of Ki-67 proliferation index. We experimentally demonstrate the superior performance of the proposed

algorithm. The future work is to improve the efficiency of the cell segmentation algorithm. The repulsive deformable model can be speeded up by considering only the local repulsion for each evolving snake, repulsive forces from all the other snakes thus will be approximately modeled with those from a few local snakes. In addition, we plan to implement this model with C programming language to reduce its running time.

REFERENCES

- [1] W. Jonat and N. Arnold, "Is the Ki-67 labelling index ready for clinical use?" *Ann. Oncol.*, vol. 22, no. 3, pp. 500–502, 2011.
- [2] H. Z. Al-Lahham, R. S. Alomari, H. Hiary, and V. Chaudhary, "Automating proliferation rate estimation from Ki-67 histology images," *SPIE*, vol. 8315, 2012.
- [3] Z. M. Mohammed, D. C. McMillan, B. Elsberger, J. J. Goings, C. Orange, E. Mallon, J. C. Doughty, and J. Edwards, "Comparison of visual and automated assessment of Ki-67 proliferative activity and their impact on outcome in primary operable invasive ductal breast cancer," *Br. J. Cancer*, vol. 106, no. 2, pp. 383–388, 2012.
- [4] J. Konsti, M. Lundin, H. Joensuu, T. Lehtimäki, H. Sihto, K. Holli, T. Turpeenniemi Hujanen, V. Kataja, L. Sailas, J. Isola, and J. Lundin, "Development and evaluation of a virtual microscopy application for automated assessment of Ki-67 expression in breast cancer," *BMC Clin. Pathol.*, vol. 11, no. 1, 2011.
- [5] P. S. Nielsen, R. Riber-Hansen, J. Raundahl, and T. Steiniche, "Automated quantification of mki67-verified Ki67 indices by digital image analysis in melanocytic lesions," *Arch. Pathol. Lab. Med.*, vol. 136, no. 6, pp. 627–634, 2012.
- [6] C. M. van der Loos, O. J. de Boer, C. Mackaaij, L. T. Hoekstra, T. M. van Gulik, and J. Verheij, "Accurate quantitation of Ki67-positive proliferating hepatocytes in rabbit liver by a multicolor immunohistochemical (IHC) approach analyzed with automated tissue and cell segmentation software," *J. Histochem. Cytochem.*, vol. 61, no. 1, pp. 11–18, 2013.
- [7] J. R. Mansfield, "Cellular context in epigenetics: Quantitative multicolor imaging and automated per-cell analysis of miRNAs and their putative targets," *Methods*, vol. 52, pp. 271–280, 2010.
- [8] C. G. Loukas, G. D. Wilson, B. Vojnovic, and A. Linney, "An image analysis-based approach for automated counting of cancer cell nuclei in tissue sections," *Cytometry A*, vol. 55, no. 1, pp. 30–42, 2003.
- [9] T. Markiewicz, C. Jochymski, R. Koktysz, and W. Kozłowski, "Automatic cell recognition in immunohistochemical gastritis stains using sequential thresholding and svm network," in *IEEE Int. Symp. Biomed. Imag. (ISBI)*, 2008, pp. 971–974.
- [10] T. Markiewicz, P. Wisniewski, S. Osowski, J. Patera, W. Kozłowski, and R. Koktysz, "Comparative analysis of methods for accurate recognition of cells through nuclei staining of Ki-67 in neuroblastoma and estrogen/progesterone status staining in breast cancer," *Anal. Quant. Cytol. Histol.*, vol. 31, no. 1, pp. 49–62, 2009.
- [11] B. Grala, T. Markiewicz, W. Kozłowski, S. Osowski, J. Słodkowska, and W. Papierz, "New automated image analysis method for the assessment of Ki-67 labeling index in meningiomas," *BMC Clin. Pathol.*, vol. 47, no. 4, pp. 587–592, 2009.
- [12] J. Słodkowska, T. Markiewicz, B. Grala, W. Kozłowski, and W. Papierz, "Accuracy of a remote quantitative image analysis in the whole slide images," *Diagn. Pathol.*, vol. 6, no. Suppl. 1, 2011.
- [13] L. H. Tang, M. Gonen, C. Hedvat, I. M. Modlin, and D. S. Klimstra, "Objective quantification of the Ki67 proliferative index in neuroendocrine tumors of the gastroenteropancreatic system: a comparison of digital image analysis with manual methods," *Am. J. Surg. Pathol.*, vol. 36, no. 12, pp. 1761–1770, 2012.
- [14] S. Fasanella, E. Leonardi, C. Cantaloni, C. Eccher, I. Bazzanella, D. Aldovini, E. Bragantini, L. Morelli, L. V. Cuorvo, A. Ferro, F. Gasperetti, G. Berlanda, P. D. Palma, and M. Barbareschi, "Proliferative activity in human breast cancer: Ki-67 automated evaluation and the influence of different Ki-67 equivalent antibodies," *Diagn. Pathol.*, vol. 6, no. S1, 2011.
- [15] E. Bernardis and S. X. Yu, "Finding dots: segmentation as popping out regions from boundaries," in *IEEE Conf. Comput. Vis. Pattern Recognit. (CVPR)*, 2010, pp. 199–206.
- [16] G. Faustino, M. Gattass, S. Rehen, and C. de Lucena, "Automatic embryonic stem cells detection and counting method in fluorescence microscopy images," in *IEEE Int. Symp. Biomed. Imag. (ISBI)*, 2009, pp. 799–802.
- [17] S. Kothari, Q. Chaudry, and M. D. Wang, "Automated cell counting and cluster segmentation using concavity detection and ellipse fitting techniques," in *IEEE Int. Symp. Biomed. Imag. (ISBI)*, 2009, pp. 795–798.
- [18] X. Lou, U. Koethe, J. Wittbrodt, and F. Hamprecht, "Learning to segment dense cell nuclei with shape prior," in *IEEE Conf. Comput. Vis. Pattern Recognit. (CVPR)*, 2012, pp. 1012–1018.
- [19] M. X. Lopez, O. Debeir, C. Maris, I. Roland, I. Salmon, and C. Decaestecker, "Ki-67 hot-spots detection on glioblastoma tissue sections," in *IEEE Int. Symp. Biomed. Imag. (ISBI)*, 2010, pp. 149–152.
- [20] S. Naik, S. Doyle, S. Agner, A. Madabhushi, M. Feldman, and J. Tomaszewski, "Automated gland and nuclei segmentation for grading of prostate and breast cancer histopathology," in *Proc. IEEE Int. Symp. Biomed. Imag. (ISBI)*, 2008, pp. 284–287.
- [21] X. Yang, H. Li, and X. Zhou, "Nuclei segmentation using marker-controlled watershed, tracking using mean-shift, and kalman filter in time-lapse microscopy," *IEEE Trans. Circuits Syst. (TCS)*, vol. 53, no. 11, pp. 2405–2414, 2006.
- [22] K. Z. Mao, P. Zhao, and P. H. Tan, "Supervised learning-based cell image segmentation for p53 immunohistochemistry," *IEEE Trans. Biomed. Eng. (TBME)*, vol. 53, no. 6, pp. 1153–1163, 2006.
- [23] G. Lin, U. Adiga, K. Olson, J. F. Guzowski, C. A. Barnes, and B. Roysam, "A hybrid 3D watershed algorithm incorporating gradient cues and object models for automatic segmentation of nuclei in confocal image stacks," *Cytometry A*, vol. 56, no. 1, pp. 23–36, 2003.
- [24] P. Yan, X. Zhou, M. Shah, and S. T. C. Wong, "Automatic segmentation of high-throughput RNAi fluorescent cellular images," *IEEE Trans. Inf. Technol. Biomed. (TITB)*, vol. 12, no. 1, pp. 109–117, 2008.
- [25] C. Jung and C. Kim, "Segmenting clustered nuclei using h-minima transform-based marker extraction and contour parameterization," *IEEE Trans. Biomed. Eng. (TBME)*, vol. 57, no. 10, pp. 2600–2604, 2010.
- [26] J. Cheng and J. C. Rajapakse, "Segmentation of clustered nuclei with shape markers and marking function," *IEEE Trans. Biomed. Eng. (TBME)*, vol. 56, no. 3, pp. 741–748, 2009.
- [27] H. C. Akakin, H. Kong, C. Elkins, J. Hemminger, B. Miller, J. Ming, E. Plocharczyk, R. Roth, M. Weinberg, R. Ziegler, G. Lozanski, and M. N. Gurcan, "Automated detection of cells from immunohistochemically-stained tissues: application to Ki-67 nuclei staining," *SPIE*, vol. 8315, 2012.
- [28] B. Parvin, Q. Yang, J. Han, H. Chang, B. Rydberg, and M. H. Barcellos-Hoff, "Iterative voting for inference of structural saliency and characterization of subcellular events," *IEEE Trans. Image Process. (TIP)*, vol. 16, pp. 615–623, 2007.
- [29] X. Qi, F. Xing, D. J. Foran, and L. Yang, "Robust segmentation of overlapping cells in histopathology specimens using parallel seed detection and repulsive level set," *IEEE Trans. Biomed. Eng. (TBME)*, vol. 59, no. 3, pp. 754–765, 2012.
- [30] O. Schmitt and M. Hasse, "Radial symmetries based decomposition of cell clusters in binary and gray level images," *Pattern Recognit.*, vol. 41, no. 6, pp. 1905–1923, 2008.
- [31] A. Hafiane, F. Bunyak, and K. Palaniappan, "Fuzzy clustering and active contours for histopathology image segmentation and nuclei detection," in *Adv. Concepts Intell. Vis. Syst. (ACIVS)*, 2008, vol. 5259, pp. 903–914.
- [32] M. Veta, A. Huisman, M. Viergever, P. J. Van Diest, and J. P. W. Pluim, "Marker-controlled watershed segmentation of nuclei in H&E stained breast cancer biopsy images," in *Proc. IEEE Int. Symp. Biomed. Imag. (ISBI)*, 2011, pp. 618–621.
- [33] Y. Al-Kofahi, W. Lassoued, W. Lee, and B. Roysam, "Improved automatic detection and segmentation of cell nuclei in histopathology images," *IEEE Trans. Biomed. Eng. (TBME)*, vol. 57, no. 4, pp. 841–852, 2010.
- [34] J. Byun, M. R. Verardo, B. Sumengen, G. Lewis, B. S. Manjunath, and S. K. Fisher, "Automated tool for the detection of cell nuclei in digital microscopic images: application to retinal images," *Mol. Vis.*, vol. 12, pp. 949–960, 2006.
- [35] Z. Bao, J. I. Murray, T. Boyle, S. L. Ooi, M. J. Sandel, and R. H. Waterston, "Automated cell lineage tracing in *Caenorhabditis elegans*," *Mol. Vis.*, vol. 103, no. 8, pp. 2707–2712, 2006.
- [36] C. Arteta, V. Lempitsky, J. A. Noble, and A. Zisserman, "Learning to detect cells using non-overlapping extremal regions," in *Int. Conf. Med. Image Comput. Assist. Intervent. (MICCAI)*, 2012, vol. 7510, pp. 348–356.
- [37] A. Santella, Z. Du, S. Nowotschin, A. K. Hadjantonakis, and Z. Bao, "A hybrid blob-slice model for accurate and efficient detection of fluorescence labeled nuclei in 3D," *BMC Bioinform.*, vol. 11, no. 1, 2010.
- [38] H. Kong, M. Gurcan, and K. Belkacem-Boussaid, "Partitioning histopathological images: an integrated framework for supervised

- color-texture segmentation and cell splitting," *IEEE Trans. Med. Imag. (TMI)*, vol. 30, no. 9, pp. 1661–1677, 2011.
- [39] A. Karsnas, A. L. Dahl, and R. Larsen, "Learning histopathological patterns," *J. Pathol. Inform. (JPI)*, vol. 2, no. 2, 2011.
- [40] A. L. Dahl and R. Larsen, "Learning dictionaries of discriminative image patches," in *Brit. Mach. Vis. Conf. (BMVC)*, 2011, pp. 1–11.
- [41] X. Liu, C. W. Harvey, H. Wang, M. S. Alber, and D. Z. Chen, "Detecting and tracking motion of myxococcus xanthus bacteria in swarms," in *Proc. Int. Conf. Med. Image Comput. Comput. Assist. Intervent. (MICCAI)*, 2012, vol. 7510, pp. 373–380.
- [42] J. Monaco, J. Hipp, D. Lucas, S. Smith, U. Balis, and A. Madabhushi, "Image segmentation with implicit color standardization using spatially constrained expectation maximization: detection of nuclei," in *Proc. Int. Conf. Med. Image Comput. Comput. Assist. Intervent. (MICCAI)*, 2012, vol. 7510, pp. 365–372.
- [43] C. Park, J. Z. Huang, J. X. Ji, and Y. Ding, "Segmentation, inference and classification of partially overlapping nanoparticles," *IEEE Trans. Pattern Anal. Mach. Intell. (TPAMI)*, vol. 35, no. 3, pp. 669–681, 2013.
- [44] N. Harder, F. Mora-Bermudez, W. J. Godinez, A. Wunsche, R. Eils, J. Ellenberg, and K. Rohr, "Automatic analysis of dividing cells in live cell movies to detect mitotic delays and correlate phenotypes in time," *Genome Res.*, vol. 19, no. 11, pp. 2113–2124, 2009.
- [45] F. Long, H. Peng, X. Liu, S. K. Kim, and E. Myers, "A 3D digital atlas of *C. elegans* and its application to single-cell analyses," *Nat. Methods*, vol. 6, no. 9, pp. 667–672, 2009.
- [46] G. Li, T. Liu, A. Tarokh, J. Nie, L. Guo, A. Mara, S. Holley, and S. T. C. Wong, "3D cell nuclei segmentation based on gradient flow tracking," *BMC Cell Biol.*, vol. 8, no. 1, 2007.
- [47] Y. Chen, E. Ladi, P. Herzmark, E. Robey, and B. Roysam, "Automated 5-D analysis of cell migration and interaction in the thymic cortex from time-lapse sequences of 3-D multi-channel multi-photon images," *J. Immunol. Methods*, vol. 340, no. 1, pp. 65–80, 2009.
- [48] F. F. Berendsena, U. A. van der Heideb, T. R. Langeraka, A. N. T. J. Kotteb, and J. P. W. Pluima, "Free-form image registration regularized by a statistical shape model: application to organ segmentation in cervical MR," *Comput. Vis. Image Understand. (CVIU)*, vol. 117, no. 9, pp. 1119–1127, 2013.
- [49] P. K. Saha, G. Liang, J. M. Elkins, A. Coimbra, L. T. Duong, D. S. Williams, and M. Sonka, "A new osteophyte segmentation algorithm using the partial shape model and its applications to rabbit femur anterior cruciate ligament transection via micro-CT imaging," *IEEE Trans. Biomed. Eng. (TBME)*, vol. 58, no. 8, pp. 2212–2227, 2011.
- [50] S. S. Chandra, J. A. Dowling, K. K. Shen, P. Raniga, J. P. W. Pluim, P. B. Greer, O. Salvado, and J. Fripp, "Patient specific prostate segmentation in 3-D magnetic resonance images," *IEEE Trans. Med. Imag. (TMI)*, vol. 31, no. 10, pp. 1955–1964, 2012.
- [51] P. K. Saha, B. Das, and F. W. Wehrli, "An object class-uncertainty induced adaptive force and its application to a new hybrid snake," *Pattern Recognit.*, vol. 40, no. 10, pp. 2656–2671, 2007.
- [52] C. Lu, S. Chelikani, X. Papademetris, J. P. Knisely, M. F. Milosevic, Z. Chen, D. A. Jaffray, L. H. Staib, and J. S. Duncan, "An integrated approach to segmentation and nonrigid registration for application in image-guided pelvic radiotherapy," *Med. Image Anal. (MIA)*, vol. 15, no. 5, pp. 772–785, 2011.
- [53] C. Lu, S. Chelikani, D. Jaffray, M. Milosevic, L. Staib, and J. Duncan, "Simultaneous nonrigid registration, segmentation, and tumor detection in MRI guided cervical cancer radiation therapy," *IEEE Trans. Med. Imaging (TMI)*, vol. 31, no. 6, pp. 1213–1227, 2012.
- [54] S. Ali, R. Veltri, J. I. Epstein, C. Christudass, and A. Madabhushi, "Adaptive energy selective active contour with shape priors for nuclear segmentation and gleason grading of prostate cancer," in *Proc. Int. Conf. Med. Image Comput. Comput. Assist. Intervent. (MICCAI)*, 2011, vol. 6891, pp. 661–669.
- [55] S. Ali and A. Madabhushi, "An integrated region-, boundary-, shape-based active contour for multiple object overlap resolution in histological imagery," *IEEE Trans. Med. Imag. (TMI)*, vol. 31, no. 7, pp. 1448–1460, 2012.
- [56] D. Comaniciu and P. Meer, "Mean shift: A robust approach toward feature space analysis," *IEEE Trans. Pattern Anal. Mach. Intell. (TPAMI)*, vol. 24, no. 5, pp. 603–619, 2002.
- [57] L. D. Cohen, "On active contour models and balloons," *CVGIP: Image Understand.*, vol. 53, no. 2, pp. 211–218, 1991.
- [58] C. Zimmer and J.-C. Olivo-Marin, "Coupled parametric active contours," *IEEE Trans. Pattern Anal. Mach. Intell. (TPAMI)*, vol. 27, no. 11, pp. 1838–1842, 2005.
- [59] J. Yang, L. Staib, and J. Duncan, "Neighbor-constrained segmentation with level set based 3-D deformable models," *IEEE Trans. Med. Imag. (TMI)*, vol. 23, no. 8, pp. 940–948, 2004.
- [60] K. Mosaliganti, A. Gelas, A. Gouaillard, R. Noche, N. Obholzer, and S. Megason, "Detection of spatially correlated objects in 3D images using appearance models and coupled active contours," in *Proc. Int. Conf. Med. Image Comput. Comput. Assist. Intervent. (MICCAI)*, 2009, vol. 5762, pp. 641–648.
- [61] O. Dzyubachyk, W. A. van Cappellen, J. Essers, W. J. Niessen, and E. Meijering, "Advanced level-set-based cell tracking in time-lapse fluorescence microscopy," *IEEE Trans. Med. Imag. (TMI)*, vol. 29, no. 3, pp. 852–867, 2010.
- [62] F. Kuhl and C. Giardina, "Elliptic fourier features of a closed contour," *Comp. Graph. Image Process.*, vol. 18, no. 3, pp. 236–258, 1982.
- [63] B. Liu, J. Huang, C. Kulikowski, and L. Yang, "Robust visual tracking using local sparse appearance model and k-selection," *IEEE Trans. Pattern Anal. Mach. Intell. (TPAMI)*, vol. PP, no. 99, pp. 1–1, 2012.
- [64] M. Aharon, M. Elad, and A. Bruckstein, "K-SVD: an algorithm for designing overcomplete dictionaries for sparse representation," *IEEE Trans. Image Process. (TIP)*, vol. 54, no. 11, pp. 4311–4322, 2006.
- [65] B. Julesz, "Texton, the elements of texture preception, and their interaction," *Nature*, vol. 290, no. 5802, pp. 91–97, 1981.
- [66] C. Schmid, "Constructing models for content-based image retrieval," in *Proc. IEEE Conf. Comput. Vis. Pattern Recognit. (CVPR)*, 2001, pp. 39–45.
- [67] F. M. Porikli, "Integral histogram: A fast way to extract histograms in cartesian spaces," in *Proc. IEEE Conf. Comput. Vis. Pattern Recognit. (CVPR)*, 2005, pp. 829–836.
- [68] J. Friedman, T. Hastie, and R. Tibshirani, "Additive logistic regression: A statistical view of boosting," *Ann. Statist.*, vol. 28, no. 2, pp. 337–407, 2000.
- [69] T. Guyon, J. Weston, S. Barnhill, and V. Vapnik, "Gene selection for cancer classification using support vector machines," *Mach. Learn.*, vol. 46, pp. 389–422, 2002.

Authors' photographs and biographies not available at the time of publication.